Received: 26 September 2024 | Revised: 7 May 2025 | Accepted: 13 May 2025

DOI: 10.1002/mrm.30588

RESEARCH ARTICLE

Magnetic Resonance in Medicine

Navigator-gated free-breathing 2D radial cardiac joint T_1–T_2 mapping

Pauline Calarnou[1] | Augustin C. Ogier[1] | Christopher W. Roy[1] | Angela Rocca[2] | Tamila Abdurashidova[2] | Jean-Baptiste Ledoux[1,3] | Roger Hullin[2] | Aurélien Bustin[1,4] | Jérôme Yerly[1,3] | Ruud B. van Heeswijk[1]

[1]Department of Radiology, Lausanne University Hospital and University of Lausanne, Lausanne, Switzerland

[2]Cardiology Service, Cardiovascular Department, Lausanne University Hospital (CHUV) and University of Lausanne (UNIL), Lausanne, Switzerland

[3]CIBM Center for Biomedical Imaging, Lausanne, Switzerland

[4]IHU LIRYC, Heart Rhythm Disease Institute, Université de Bordeaux – INSERM, Pessac, France

Correspondence
Ruud B. van Heeswijk, Department of Radiology, Lausanne University Hospital and University of Lausanne, BH/08/084 Rue du Bugnon 46, 1011 Lausanne, Switzerland.
Email: ruud.mri@gmail.com

Funding information
Schweizerischer Nationalfonds zur Förderung der Wissenschaftlichen Forschung, Grant/Award Numbers: 32003B_182615, CRSII5_202276, PZ00P3_202140

Abstract

Purpose: To implement a navigator-gated free-breathing 2D radial joint T_1–T_2 mapping technique for the myocardium at 3T, and to characterize the impact of the navigator rejection on the precision and accuracy of the T_1 and T_2 maps.

Methods: The proposed technique, named PARMANav (for PArametric Radial Mapping with Navigator gating), collects 25 lung–liver navigator-gated electrocardiogram (ECG)-triggered single-shot radial gradient-recalled echo (GRE) images with five magnetization preparations. Source images were reconstructed using compressed sensing. Extended-phase-graph simulations were used to generate an acquisition-specific joint T_1–T_2 dictionary. The impact of the number of rejected navigators on the relaxation times was assessed in numerical simulations. The influence of the navigator acceptance window width (NAWW) and heart rate on the relaxation times was assessed in phantom studies, 10 healthy volunteers, and 3 patients. The relaxation times were compared to routine T_1 and T_2 mapping values.

Results: The numerical simulations showed negligible dependence on the number of rejected navigators (<6% T_1–T_2 variation). In the phantom, PARMANav T_1–T_2 values were stable across heart rates: the T_1–T_2 coefficient of variation (CoV) was <3%. As expected from literature, in-vivo PARMANav T_1–T_2 values were higher than routine values ($T_1 = 1331 \pm 53$ ms, $T_2 = 46.1 \pm 2.5$ ms vs. $T_1 = 1095 \pm 81$ ms, $T_2 = 38.7 \pm 2.9$ ms, $p < 0.001$), while the PARMANav T_2 CoV was significantly reduced. No myocardial T_1–T_2 values or CoV trend was observed for the different NAWW. Feasibility in patients was demonstrated, where high-quality maps were obtained.

Conclusion: PARMANav allows for precise and accurate joint T_1–T_2 mapping without requiring breath holding. Through-plane motion artifacts were avoided with a navigator that did not impact the accuracy or precision of the resulting maps.

KEYWORDS

cardiac magnetic resonance, MR fingerprinting, myocardial tissue characterization, parametric mapping, respiratory navigator gating, T1 mapping, T2 mapping

1 | INTRODUCTION

The T_1 and T_2 relaxation times of the myocardium strongly correlate with myocardial fibrosis and edema, respectively.[1] Over the past decade, multiparametric mapping techniques such as MR fingerprinting,[2,3] MR multitasking[4] and mSASHA[5] have emerged as promising techniques for quantitative tissue characterization of the myocardium.[6,7] Multiparametric mapping has shown great performance in overcoming several limitations of conventional T_1 and T_2 mapping techniques, such as the need for multiple breath holds and the presence of confounding factors (e.g., B_1 inhomogeneities, magnetization transfer, or the influence of T_1 and T_2 relaxation on each other). This has resulted in improved accuracy, repeatability, and robustness in the assessment of myocardial tissue characteristics.[8] The first clinical studies have now shown the feasibility and efficiency of these techniques in patients with ischemic and nonischemic cardiomyopathy.[9–11]

Most of these multiparametric mapping techniques rely on varying the magnetization with different preparation modules in order to induce a unique signal time course that depends on underlying relaxation parameters of interest. The acquired data are fitted pixel-by-pixel with an analytical equation,[12–14] or, more recently, matched with an entry of a dictionary of simulated time courses. The latter has the advantage that imperfections of the technique can also be easily modeled in the simulated time courses[15] and has already been demonstrated to results in improved consistency of the myocardial T_1 values compared to analytical fitting.[16,17] The acquired data can be either gridded or reconstructed using compressed sensing (CS).[18] Model-based reconstruction[19] can also be used for multiparametric mapping, by using physics-based property of the magnetization as a prior in the CS reconstruction.

These methods have previously been developed for breath-held 2D[2] and 3D[13] and free-breathing 3D[20] joint T_1–T_2 mapping of the myocardium at 1.5 and 3T. Indeed, myocardial mapping methods tend to be breath-held acquisitions. These sequences are therefore susceptible to motion artifacts due to imperfect breath holds, especially in protocols that require repeated breath holds, which also makes them unsuitable for patients with dyspnea. To enable free-breathing acquisitions, self-navigation[21,22] or image navigators can be used for 3D imaging, while a lung–liver navigator[23–25] can be added to track the diaphragm position and limit through-plane motion for 2D imaging. Free-breathing methods based on slice-tracking performed with a lung–liver navigator[25] or based on a pilot tone pre-scan[26] were also applied for cardiac T_1 mapping. Retrospective motion correction can address in-plane motion; however, without the use of a navigator, it cannot account for through-plane motion.[27] This may be critical in case of focal disease, where through-plane motion risks causing apparent elevated values in healthy tissues or apparent normal values in a lesion.

Lyu et al.[28] recently proposed a free-breathing Cartesian technique for simultaneous native T_1 and T_2 myocardial mapping at 3T, using a lung–liver navigator. In their approach, the navigator is used for slice tracking, and not for gating. Prospective respiratory motion correction is thus performed by adjusting the imaging plane in real-time as a function of the position of the lung–liver interface, resulting in a 100% navigator efficiency. Our proposed technique instead uses both tracking and gating, which reduces the efficiency but also reduces the through-plane motion on the image due to imperfect slice tracking. Indeed, respiratory motion tracking relies on an experimentally determined tracking factor that links the motion of the diaphragm and the heart.[29] This scaling or tracking factor has been shown to be an imperfect approximation, as it assumes a linear correlation with the position of the diaphragm and varies across patients, except in the case of small acceptance windows.[30] However, navigator-gated multiparametric mapping raises new challenges, since the navigator rejection significantly influences the magnetization evolution. Consequently, the influence of parameters such as the navigator acceptance window width (NAWW) on the which relaxation time accuracy and precision should be thoroughly examined.

The goal of this study was therefore to develop, optimize, and validate a navigator-gated free-breathing 2D radial sequence for accurate and precise joint T_1–T_2 mapping of the myocardium at 3T. The proposed method was validated through numerical simulations, phantom studies, and tests on healthy volunteers. Its preliminary clinical feasibility was also assessed in patients with cardiac disease.

2 | METHODS

2.1 | PARMANav pulse sequence design

The proposed pulse sequence (named PARMANav for PArametric Radial MApping with Navigator gating) collects 25 navigator-gated free-breathing electrocardiogram (ECG)-triggered magnetization-prepared single-shot gradient-recalled echo (GRE) images. The single-shot 2D GRE images are acquired as 45 radial lines with a continuous golden-angle trajectory,[31] resulting in each image being unsampled at 15% of the Nyquist rate. Five different magnetization preparations were used to sensitize the contrast to both T_1 and T_2 relaxation:[20,32] an adiabatic inversion pulse (a 5120 ms hyperbolic tangent), no

preparation, and three different adiabatic T_2 preparation (T_2-prep) modules ($TET_{2\text{-prep}} = 23/45/70$ ms) (Figure 1A). This set of five preparations was then repeated five times, to introduce more contrast variations. The number of repetitions was chosen heuristically.

Respiratory motion was tracked using a lung–liver navigator[23] before each preparation module (Figure 1C). A NAWW between ±4 and ± 32 mm was chosen, and slice tracking was activated.[29] When the navigator position is outside the acceptance window, neither the preparation module nor the image acquisition are activated during that heartbeat, which significantly impacts the magnetization evolution and the corresponding simulated dictionary. If the preparation modules were not deactivated during navigator rejection, the exact timing of their execution would be uncertain due to heart rate variability, potentially resulting in T_1–T_2 inaccuracies.

All data were acquired on a 3T clinical scanner (Magnetom PrismaFit, Siemens Healthineers, Forchheim, Germany) with matrix size = 192 × 192, pixel size = $(1.56\text{ mm})^2$, flip angle = 12°, bandwidth = 789 Hz/pixel, slice thickness = 8 mm, TR = 3.49 ms, and TE = 1.56 ms, inversion time TI = 68.28 ms (for the image directly after the inversion), acquisition window duration = 151 ms. For all acquisitions we used a 34-channel chest-spine coil array, of which the 30 closest elements to the FOV were used for our study.

2.2 | Image reconstruction and dictionary generation

Images were reconstructed from the undersampled data using CS with total variation regularization in the spatial dimension and local low rank regularization along the contrast dimension[33]:

$$\hat{\mathbf{x}} = \underset{\mathbf{x}}{\operatorname{argmin}} \|\mathbf{FCx} - \mathbf{y}\|_2^2 + \lambda_S \|\nabla_s \mathbf{x}\|_1 + \lambda_C \sum_{i>1} \|\mathbf{L}_i \mathbf{x}\|_* \quad (1)$$

where $\hat{\mathbf{x}}$ is the reconstructed image, $\mathbf{F}$ is the nonuniform fast Fourier operator, $\mathbf{C}$ is the coil sensitivity, $\mathbf{y}$ refers to the acquired k-space, ∇_s is the first-order difference operator along the spatial dimension, $\mathbf{L}_i$ is the operator that extracts the i-th spatial patch of size 6 × 6 × 6 pixels from $\mathbf{x}$ and form a Casorati matrix with the contrast dimension, $\|\cdot\|_*$ is the nuclear norm, and λ_S and λ_C are the corresponding regularization weights along the spatial and contrast dimensions, respectively. After initial testing in multiple datasets (not reported here), λ_S and λ_C were set to 0.03 and 0.06, respectively, as an optimum balance between undersampling artifact removal and image blurring.

An acquisition-specific dictionary of the evolution of the magnetization was simulated for each acquisition using the extended phase graph (EPG)[34] formalism for a range of T_1 (40:10:3000 ms) and T_2 (20:1:100; 102:2:230 ms) values in Matlab (R2021b, The Mathworks, Natick, Massachusetts, U.S.A) (Figure 1E). The simulation incorporates 50 isochromats to account for slice profile correction, as well as an inversion inefficiency correction.[15]

Since the timing of the sequence is acquisition-specific due to the variations in heart rates and accepted navigators, it was extracted from the raw data and fed into the simulation framework directly. Using the absolute readouts timing extracted from the raw date along with pre-defined parameters (e.g., TI, spoiler duration etc.), the time course of an individual acquisition was established. The magnetization was simulated at the center of each echo, and the average signal of each radial single-shot image was stored, resulting in a $25 \times 42\,161$ ($T_2 > T_1$ cases excluded) matrix of simulated complex signals that forms the dictionary.

A model-based non-rigid image registration similar to Bustin et al.[35] was applied to account for residual in-plane motion resulting from residual differences in the respiratory and cardiac phase, together with the strong contrast variations in these images (Figure 1F). To handle contrast variations in series of quantitative MRI images, a pairwise approach is often employed, using a mutual information metric. This metric is effective because it is resilient to intensity change in the images, but the pairwise approach requires choosing a reference image, which can significantly impact the result of the registration.[36] In the proposed approach, all the images are registered to a corresponding synthetic image with the same contrast and an averaged motion state. Briefly, after the generation of a dictionary as described above, a first map is produced by pixel-wise dictionary matching (i.e., without any motion correction). This dictionary matching was then reversed to obtain synthetic images with the same contrast as the corresponding source images, but with the same averaged motion state for all synthetic images. Next, a non-rigid optical-flow-based motion correction[37] was applied between the pairs of synthetic and source images with the same contrast, ensuring alignment to an average motion state. Registered maps were then obtained by repeating the pixel-wise dictionary matching on the registered images with a dot product. While the registration process introduces some blurring in the final maps, this approach significantly reduces the errors that would arise from fitting models on non-aligned data.

The offline reconstruction and dictionary simulations were performed using Matlab on a Linux workstation with two 24-core central processing units (CPUs; Intel Xeon

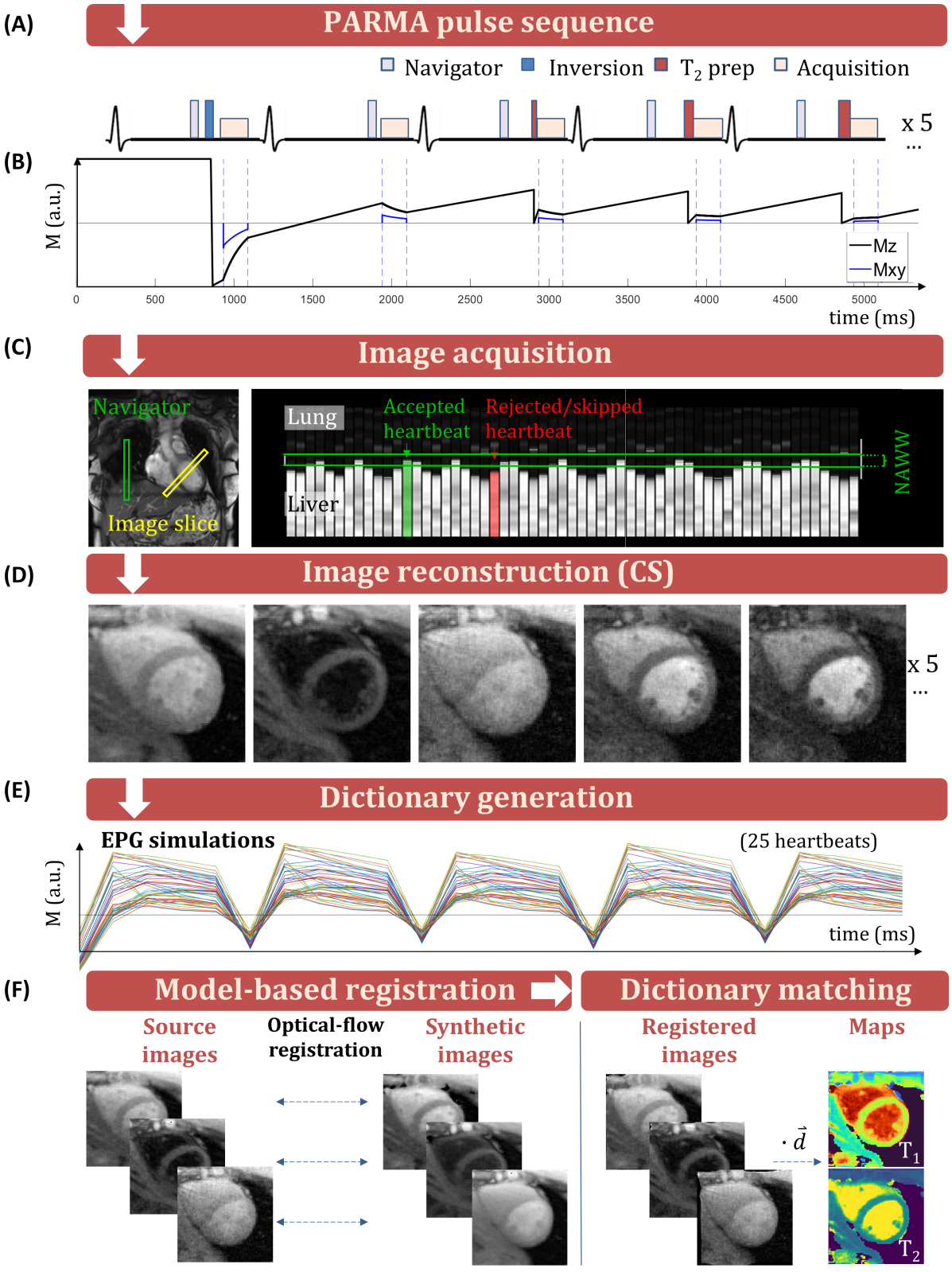

FIGURE 1 PArametric Radial Mapping with Navigator gating (PARMANav) pulse sequence, image reconstruction, and mapping. (A) Pulse sequence diagram. The images are acquired during 25 heartbeats, using inversion pulses and three different T_2-prep modules. (B) Magnetization evolution of the myocardium across five cardiac cycles. (C) Illustration of the placement of the navigator and image slice with a trace of the navigator with the acceptance window as two parallel green lines. (D) Images from the first five cardiac cycles in a healthy volunteer, reconstructed using compressed sensing. (E) Simulated signals of the dictionary across 25 heartbeats obtained using extended phase graph (EPG) simulations. (F) Model-based motion correction between source and synthetic images obtained with the dictionary. The final maps are obtained by computing the dot-product between the registered images and the dictionary $\vec{d}$.

Gold 6248R; Intel, Santa Clara, CA, USA), 1.5 TB of RAM; an RTX A6000 GPU (Nvidia, Santa Clara, CA, USA) was used in the computation of the non-uniform fast Fourier transform. The CS reconstruction was performed in less than 10 min, and the dictionary was simulated in approximately half an hour.

2.3 | Numerical simulations

A numerical simulation of the human torso was developed to simulate the acquisition of PARMANav images, inspired by previously described approaches.[38,39] The scan-specific dictionary of any in-vivo PARMANav acquisition can be used as input to obtain ideal undersampled k-space data with a magnetization time course that corresponds to the in-vivo acquisition timing.

To assess the influence of significant timing variability due to navigator rejections, a dictionary was generated for each of the mid-ventricular short-axis PARMANav acquisition timings of the ten healthy volunteers described below. Published T_1 and T_2 values were used for the digital phantom tissues (Table S1). This resulted in a simulated signal at the center of each of the 25×45 (heartbeats $\times$ readout lines) =1125 readouts for each tissue type and timing. This dictionary was then used to generate "ground truth" images at each of the 1125 time points of the acquisition timing. In each ground truth image, a single line of the golden angle trajectory was sampled, resulting in a simulated undersampled k-space. To ensure a realistic noise level, Gaussian noise was generated with an amplitude based on the noise characterization pre-scan, collected along the raw data of three healthy participants. Here, the noise SD (σ_{noise}) was determined from both the real and imaginary noise components in all coil elements in each participant's pre-scan. This σ_{noise} was scaled relative to the maximum k-space intensity (k_{max}) of the PARMANav image in that participant to obtain their ratio $R = \sigma_{noise}/k_{max}$. R was averaged for the three participants. The maximum k-space intensity of the numerical simulation was then multiplied by R to find σ_{noise} for the simulation, and the corresponding noise was added to each individual coil elements. This k-space, with and without the Gaussian noise, was then subjected to the CS image reconstruction described above, and pixel-wise dictionary matching was performed as described earlier to generate parametric maps. For each acquisition timing, the number of navigator rejections was extracted as the number of skipped heartbeats.

The impact of the navigator rejection (i.e., skipped heartbeats) was then characterized by calculating the difference between the resulting myocardial T_1 and T_2 values and the input values as a measure of the accuracy. The myocardial coefficient of variation (CoV, the ratio of the SD and the mean value) was used to quantify the influence of the skipped heartbeats on the precision.

2.4 | Phantom study

The "ISMRM/NIST"[40] phantom (Premium System 130, CaliberMRI, Boulder, USA) was scanned to evaluate the accuracy of PARMANav (with matrix size = 192 $\times$ 192, pixel size = $(1.56\,mm)^2$, slice thickness = 8 mm, TR = 3.49 ms, and TE = 1.56 ms) with simulated ECG triggering. Clinical routine T_1 and T_2 maps (pixel size = $(1.4–1.9\,mm)^2$, slice thickness = 8 mm) were acquired using 5(3)5 and 4(1)2(1)3 MOLLI,[41] referred to as MOLLI preGd and postGd, respectively, and T_2-prep balanced steady-state free precession (bSSFP) T_2 mapping,[24,42] respectively. To establish the accuracy of the technique, a linear regression was performed between the resulting relaxation times and those obtained with the gold-standard inversion-recovery spin-echo and spin-echo techniques. This experiment was repeated for five different simulated heart rates (40, 60, 80, 100, and 120 bpm), and the T_1 and T_2 values were recorded across the simulated heart rates.

2.5 | Healthy volunteer study

All human studies were approved by the local ethics committee (CER-VD approval 2021–00697), and written informed consent was given by all participants. In-vivo experiments were performed in 10 healthy volunteers (age = 26.9 ± 2.5 years, 3 women). To study the impact of the NAWW of the lung–liver navigator, a mid-ventricular short-axis PARMANav was acquired with four different NAWW (±4 mm, ±8 mm, ±16mmm, and ± 32 mm). The volunteers were instructed to breathe normally. For NAWW = ±8 mm additional basal and apical short-axis slices were acquired. Breath-held MOLLI pre and T_2-prep bSSFP were acquired in mid-ventricular short-axis as routine T_1 and T_2 mapping methods, respectively. Acquisition times for the different NAWW were also reported.

2.6 | Preliminary patient study

PARMANav was acquired in three patients (age = 59 ± 3.6 years, three men) both in native contrast and post gadolinium-based contrast-agent injection (approximately 10 min after the injection of 0.2 mmol/kg bodyweight gadobutrol, Gadovist, Bayer AG, Leverkusen, Germany). In each patient, a basal, mid, and apical short-axis slices

were acquired. The patients were a heart transplant recipient at routine checkup with cardiac allograph vasculopathy and an old coronary dissection, and two patients with heart failure with preserved ejection fraction.

PARMANav-based extracellular volume fraction (ECV) maps were obtained with the pre- and post-contrast T_1 maps and were registered using the corresponding T_2 maps with affine mutual-information motion correction. ECV was calculated pixel-by-pixel,[43] where the T_1 value of the blood was obtained by manually segmenting a region of interest in the left-ventricular blood pool, and the hematocrit value was obtained from routine laboratory blood work performed at 9 a.m., 8 h: 25 min ± 3 h: 04 min before the MR scan, in a supine position after several minutes of rest.[44]

2.7 | Statistics

In the numerical simulations, the coefficient of determination (R^2) of the linear regression between the number of skipped heartbeats and the T_1–T_2 values and CoV was used to check for any linear dependence between those parameters.

The agreement between the measured and gold-standard values in the phantom was assessed through both the slope and R^2 of the linear regression. The CoV of the phantom compartment relaxation values over the different heart rates was reported.

In the healthy volunteers, regions of interest were manually segmented on the T_1–T_2 maps in 16 segments according to the American Heart Association (AHA) model.[45] The mean value and CoV (as a measure of precision) of these segments and of the entire myocardium were extracted for the four NAWWs and the two routines methods. Their differences were tested with a repeated-measures analysis of variance (ANOVA) with post-hoc Tukey analysis. The segmental T_1–T_2 means and SDs across the healthy volunteers were reported in a bullseye plot.

3 | RESULTS

3.1 | Numerical simulations

Highly precise maps that matched the ground-truth T_1 and T_2 values of the digital phantom were obtained for all NAWWs (Figures 2 and S1). The relative difference between the resulting myocardium T_1 value and the input T_1 value remained below 1%. No strong trend could be observed with the number of skipped heartbeat ($R^2 = 0.01$), even if the difference appears to be somewhat reduced for the highest numbers of skipped heartbeats.

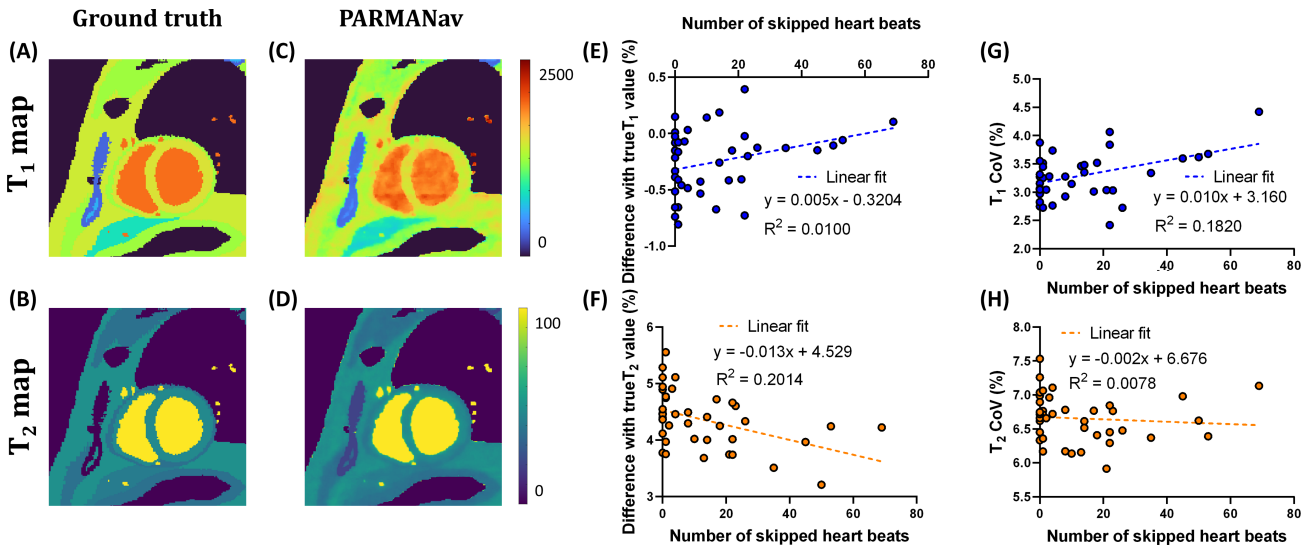

FIGURE 2 Maps of the numerical simulations and the influence of skipped heartbeats. (A, B) Input source T_1 and T_2 maps. (C, D) Example resulting T_1 and T_2 maps after the simulated acquisition and reconstruction. (E, F) Difference between the myocardial T_1 and T_2 values after the simulated acquisition and the input values as a function of the number of skipped heartbeats. The T_1 difference was very low (less than 1%), and no clear trend was observed as the number of skipped heartbeats increases ($R^2 = 0.01$). While the T_2 difference was on average higher, there was only a ~4% T_2 variation over the entire range of heartbeats. (G, H) T_1 and T_2 CoV in the myocardium as a function of the number of skipped heartbeats; there was negligible impact ($R^2 = 0.18$ for T_1 and $R^2 = 0.007$ for T_2).

The T_2 value of the myocardium was matched with high precision, and a similar correlation with the number of skipped heartbeats was observed ($R^2 = 0.20$). The T_1 and T_2 CoV were independent of the number of skipped heartbeat ($R^2 = 0.18$ and $R^2 = 0.01$, respectively). The absence of noise did not have large impact on those results (Figure S1).

3.2 | Phantom study

The PARMANav phantom measurement demonstrated good concordance with the reference for both the T_1 and T_2 relaxation times (Figure 3). The slope of the correlation plot was closer to identity than routine techniques (1.072 vs. 0.76 and 0.83, for PARMANav and MOLLI pre and post T_1, respectively, and 1.082 vs. 0.460 respectively for T_2) at 60 bpm.

The heart rate dependence study showed consistent results across the different heart rates for our proposed technique (Figure 3E–G) ($R^2 > 0.99$ for all heart rates and CoV of the vials <3% over the heart rates). MOLLI pre and post results are shown without the lower and higher T_1 values where its analytical fit failed. However, for the lowest T_1 phantom compartment, the resulting T_1 values were not constant across heart rates. PARMANav was robust to the change (i.e., CoV <3%) in heart rate for a larger range of T_1 and T_2 values.

3.3 | Healthy volunteer study

In all 10 healthy volunteers, PARMANav resulted in precise T_1 and T_2 maps for all NAWWs (Figure 4). The myocardial PARMANav T_2 CoV was lower than the routine T_2 CoV, while the T_1 and T_2 global and segmental means were significantly higher than those of the routine methods (Figure 5). The only significant T_1 or T_2 difference observed between the different PARMANav acquisitions was between myocardial T_1 value of NAWW = ±4 mm and NAWW = ±8 mm (Figure 4B). The spread of T_1 values across volunteers was smaller for PARMANav than for the routine method, except for the values obtained with the large NAWW of ±32 mm ($IQRT_1 = 41,57$ 112 and 163 ms for NAWW of ±4, ±8, ±16 and ± 32 mm, respectively, vs. 135 ms for MOLLI). This discrepancy may be caused by through-plane motion, as abnormally low T_1 values were measured at NAWW = ±32 mm in the two volunteers that exhibited a deep breathing pattern (Figure 6).

The T_1 CoV at NAWW = ±4 and ± 8 mm were significantly lower that the CoV at NAWW = ±16 mm ($p = 0.03$

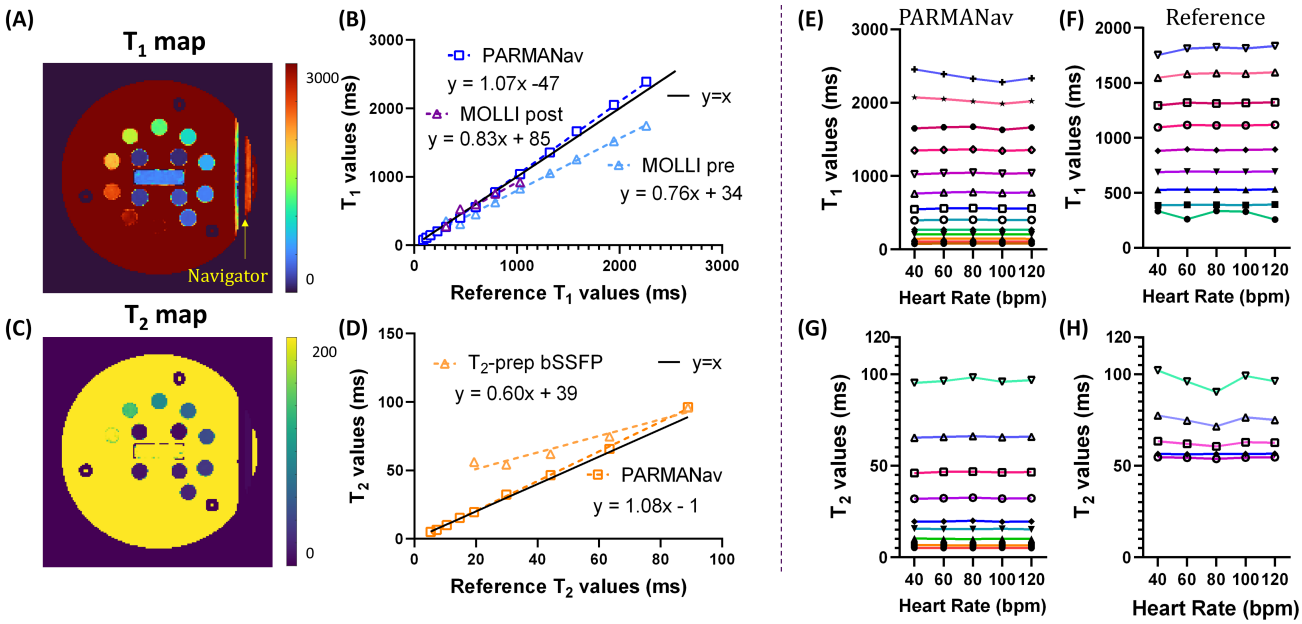

FIGURE 3 Accuracy of PARMANav T_1 and T_2 maps in the ISMRM-NIST phantom compared to spin-echo reference values and across heart rates. (A) T_1 map of the phantom obtained with PARMANav. (B) Linear regression plots of T_1 values and the clinical routine 5(3)3 and 4(1)2(1)3 MOLLI (MOLLI preGd and postGd, respectively) versus gold-standard inversion recovery spin echo (IR-SE). (C) T_2 map of the phantom obtained with PARMANav. (D) Linear regression plots of T_2 values and the clinical routine T_2-prep balanced steady-state free precession (bSSFP) in the phantom in the clinically relevant range versus gold-standard SE. (E) T_1 values measured in the phantom across five simulated heart rates for PARMANav. (F) Similar plot for the T_1 values obtained with MOLLI. (G) Similar plot for the T_2 values obtained with PARMANav. (H) Similar plot for the T_2 values obtained with T_2-prep bSSFP.

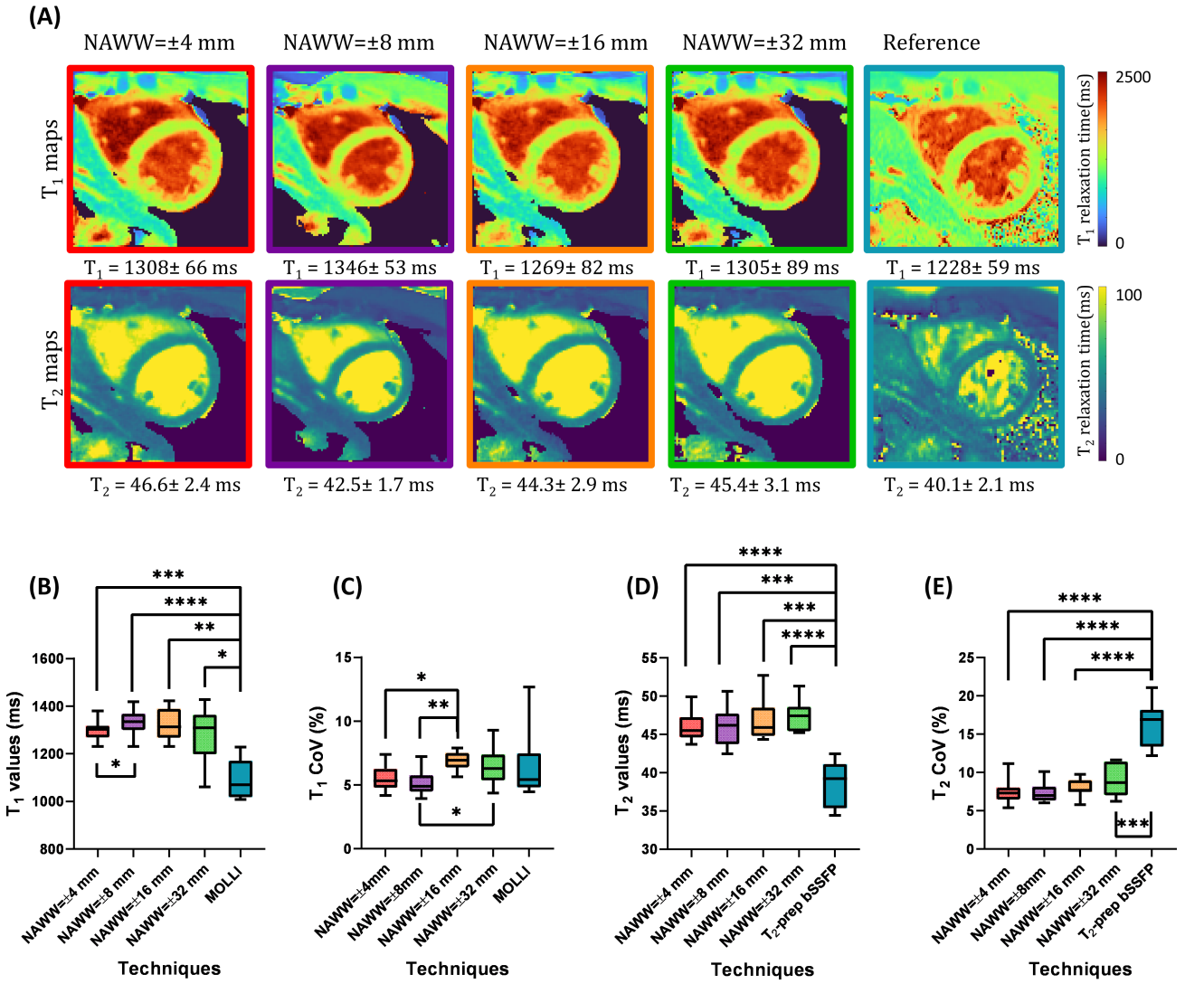

FIGURE 4 PARMANav T_1 and T_2 maps and values for the healthy volunteers. (A) Representative maps of a healthy volunteer for the different NAWWs compared to routine techniques, with the myocardial relaxation time and SD underneath. (B) Myocardial T_1 values for the four NAWWs, compared to MOLLI T_1 values. (C) Myocardial T_1 CoV for the four NAWWs, compared to MOLLI T_1 CoV. (D) Myocardial T_2 values for the four NAWWs, compared to T_2-prep balanced steady-state free precession (bSSFP) T_2 values. (E) Myocardial T_2 CoV for the four NAWWs, compared to T_2-prep bSSFP T_2 CoV. *$p < 0.05$; **$p < 0.01$; ***$p < 0.001$; ****$p < 0.0001$.

and $p = 0.01$, respectively), although no difference could be observed between PARMANav and MOLLI T_1 CoV (Figure 4C). PARMANav T_2 CoV were significantly lower than those of the routine technique ($p < 0.004$, Figure 4E).

The difference in acquisition time between the narrowest and widest NAWW was 2.15 times, or from 25 ± 4 s to 53 ± 23 s (Figure S2).

No change in relaxation time was observed across the different NAWWs, which from ±4 to ±16 mm all resulted in visually artifact-free high-quality maps (Figure 4A). In several volunteers ($n = 2$), a reduction in the visible thickness of the myocardium in the lateral part could be observed for NAWW = ±32 mm.

3.4 | Patient study

PARMANav was successfully acquired in the three patients, resulting in high-quality maps (Figure 7). The ECV maps demonstrated two clinically confirmed old infarctions: one associated with ischemic heart disease in Patient 1, and another resulting from a coronary artery dissection in Patient 3. Elevated regions of interest were manually segmented and compared to the remote myocardium in the three slices, resulting in an ECV of 65% and 73% in the elevated region, and 40% and 44% in the rest of the myocardium, for Patient 1 and 3, respectively.

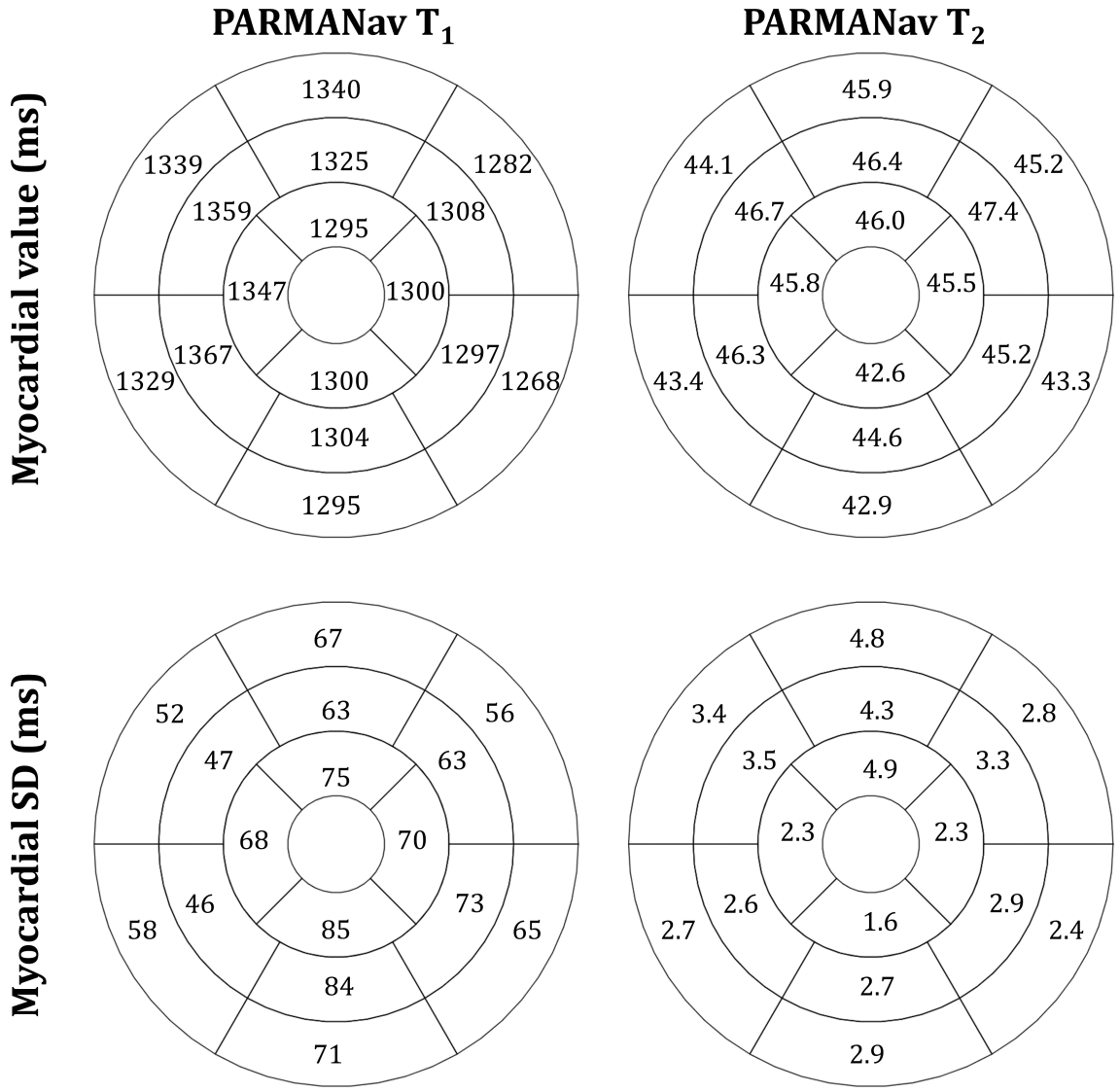

FIGURE 5 Bullseye plot of the PARMANav T_1 and T_2 maps. The mean and SD of the values across the 10 healthy volunteers for a NAWW of ±8 mm for the 16 American Heart Association (AHA) segments in the three short-axis slices.

4 | DISCUSSION

In this work, a navigator-gated free-breathing 2D radial technique was developed and characterized for joint T_1–T_2 mapping of the myocardium at 3T. Numerical simulations demonstrated that the estimated T_1 and T_2 values in the myocardium were not significantly impacted by the number of skipped heartbeats due to navigator rejection. The different image reconstruction steps furthermore only resulted in a slight but consistent increase in T_1 value, and a negligible decrease in T_2 value. The presence or absence of noise did not impact this tendency, indicating that the CoV is dominated by the effect of the reconstruction. The accuracy and robustness to heart rate variability of PARMANav relaxation times were then demonstrated in a mapping phantom, showing consistent agreement with the gold-standard values. The routine T_1 mapping technics MOLLI failed for the central four spheres of the NIST phantom, most likely due to the very short T_2 values (5, 7, 10, and 15 ms). A phantom characterization with a variable heartrate could be of interest but was not performed here, as we believe that respiratory gating introduces the most significant variability compared to heart rate fluctuations.

The study in healthy subjects showed a T_1 and T_2 bias compared to clinical routine techniques, which was expected as both techniques are known to underestimate these values.[46] Reducing this bias has been the subject of several studies,[24,47] but in this work the comparison was only made with the version that is used in most clinical routines (i.e., MOLLI). Feasibility was demonstrated in the

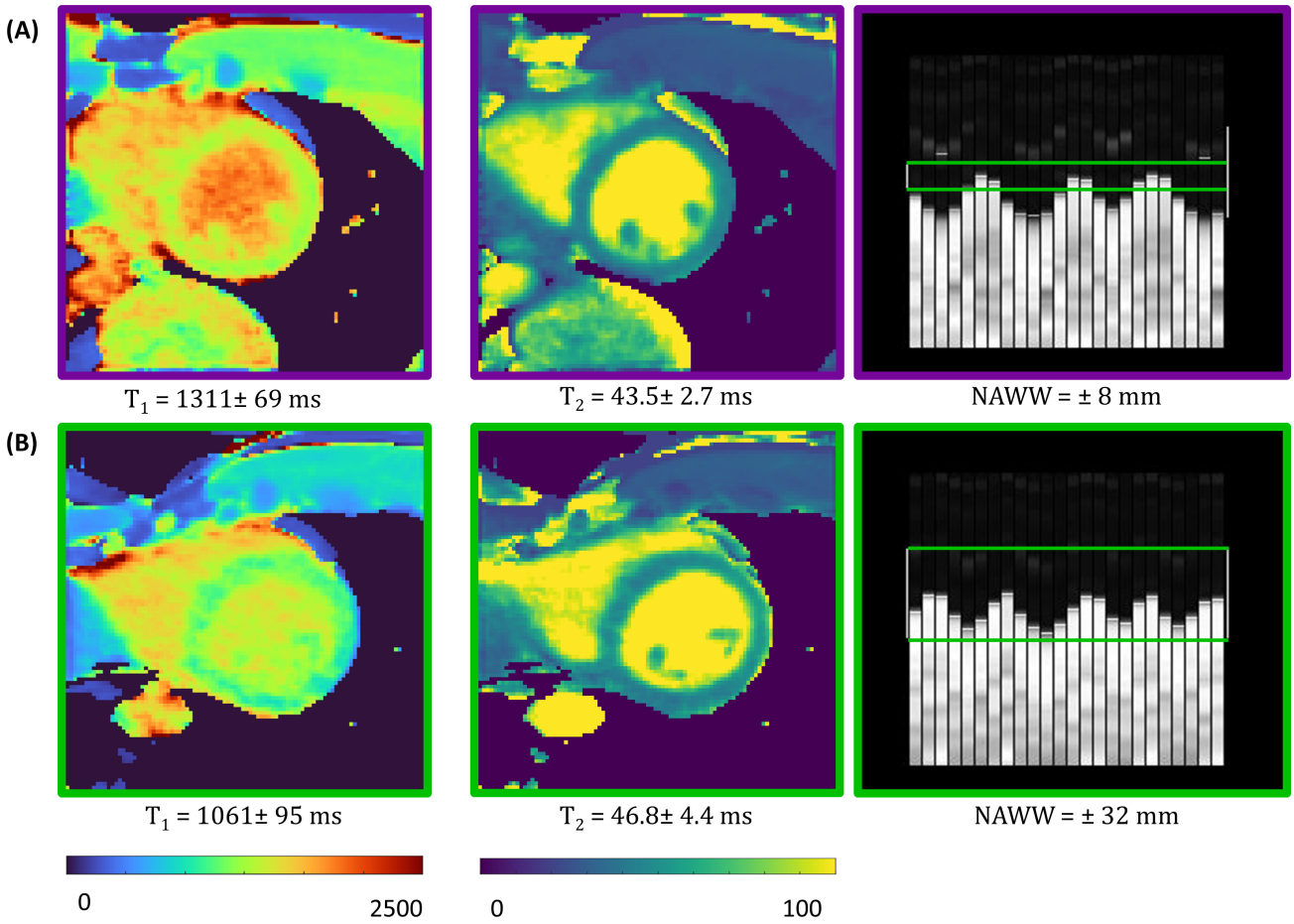

FIGURE 6 Anecdotal evidence of the influence of large through-plane motion on the maps. (A) T_1 and T_2 map of a healthy volunteer with NAWW = ±8 mm, with a part of the corresponding navigator plot. The acceptance window is represented in green. Only a small part of the lung–liver transitions was within this window and, thus, accepted for data acquisition. The T_1 and T_2 values of the segmented myocardium were reported under the images and were within a normal range. (B) T_1 and T_2 maps of the same healthy volunteer with NAWW = ±32 mm, with the corresponding partial navigator plot, which shows that all lung–liver transitions were accepted. The T_1 values were abnormally low, which may be caused by through-plane motion that results in different tissues being excited at each respiratory state. It should be noted that this volunteer exhibited deeper breathing pattern than most others.

patient setting for native maps and post-gadolinium injection, where we reported high-quality maps and were able to characterize an old infarct.

All patient ECV values were relatively high(>30%),[46] suggesting the presence of interstitial fibrosis. Light streaking-like artifacts were observed in the heart transplant recipient, which might be caused by the proximity of steel sternal wires, or it might be a partial-volume effect due to the low basal location of the slice. Alternative techniques that lower the influence from regions outside the heart, such as ROVir,[48] could be explored in this patient population in future studies. PARMANav ECV will also need to be obtained in healthy volunteers to establish the sensitivity and the specificity of the EVC mapping. Hematocrit values have been shown to vary with body posture, so Engblom et al.[49] recommended performing hematocrit measurements at the end of the MRI exam, rather than before, as previously recommended.[46] In our study, blood samples were drawn several hours before the exam in a supine position after several minutes of rest, which might thus lead to a slight ECV underestimation. Simultaneously, hematocrit levels also peak in the morning,[50] which could also result in an underestimated ECV value. Nevertheless, since blood drawing and exam times were fixed, any resulting bias would be consistent across these three subjects.

3D joint myocardial T_1–T_2 mapping (3D-QALAS) was initially developed by Kvernby et al.,[13] while more recently for example a Cartesian dictionary-based joint myocardial T_1–T_2 mapping technique was proposed by Henningsson mapping at 1.5T,[32] and a multiparametric version of SASHA (mSASHA) was introduced by Chow et al. for cardiac T_1 and T_2 quantification at 3T.[5] These techniques all require breath-holds of 10 or more heartbeats.

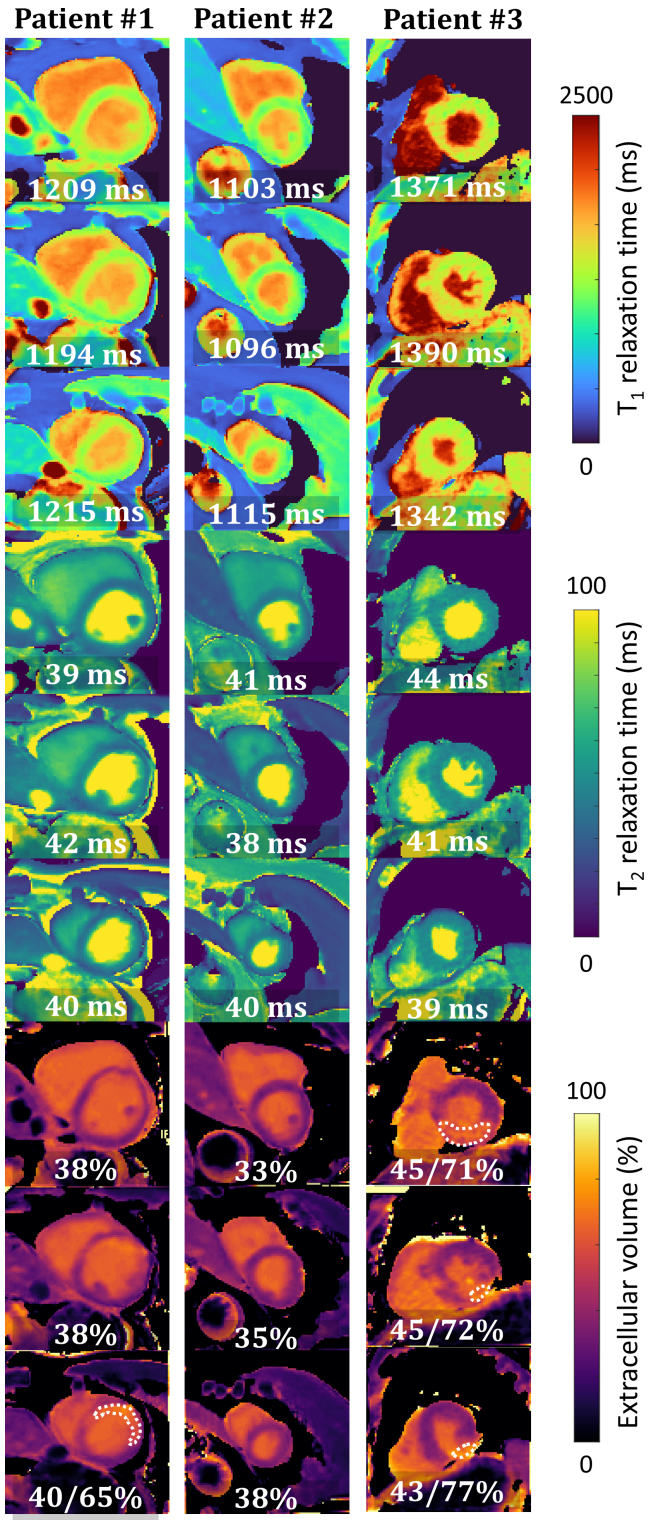

FIGURE 7 Parametric patient maps obtained in patients. Patients 1 and 2 suffered from heart failure with preserved ejection fraction, and Patient 3 was a heart transplant recipient with cardiac allograft vasculopathy. Old infarctions due to ischemic heart disease and a coronary dissection can be observed in the ECV maps of Patients 1 and 3, respectively.

By including a lung–liver navigator, we could prolong our acquisition to 25 heartbeats without compromising on the through-plane motion or feasibility in patient with limited breath-hold capacity. This should also facilitate the application in patients, as breath holding can be challenging. Our dictionary was obtained with EPG simulation for each acquisition. Free-breathing Cartesian simultaneous native T_1 and T_2 with a lung–liver navigator mapping has also been recently proposed for myocardial mapping at 3T by Lyu et al.[28] In this work, the use of navigator tracking (but not gating) offered a 100% navigator efficiency. On the other hand, real-time slice tracking has several limitations, such as the assumption of a linear relation between the diaphragm and the heart motion, and the use of a single tracking factor that does not apply to all patients.[30] In the present work, using only real-time slice tracking (i.e., using a NAWW that encompasses all respiratory positions) was not sufficient in two subjects and resulted in abnormally low T_1 values. This did not happen when navigator gating was added. Nevertheless, imperfect slice tracking may still introduce errors, as residual through-plane motion alters the magnetization history of the imaged slice, which is not accounted for in the dictionary.

The PARMANav relaxation times of the myocardium were consistent with previous studies by Chow et al.[5] for the T_1 values. On the other hand, the reported T_2 are higher, similar to what was reported by Kvernby et al.[13] The precision reported for the PARMANav myocardial relaxation times were similar to that of MOLLI and significantly higher than that of T_2-prep bSSFP.

Beyond the presented phantom and healthy volunteer comparison to spin echo and MOLLI, a direct comparison of in-vivo T_1 and T_2 values obtained with different techniques in different centers is challenging, since these values were obtained in different cohorts, scanners, and sites. For T_1 mapping, SASHA has been shown to have higher accuracy than MOLLI, but lower precision.[51] While SASHA should thus be more reproducible between scanners and vendors, this lower precision usually leads to MOLLI being preferred.[52] Based on the results in this study, PARMANav can be preliminarily expected to approach the high accuracy of SASHA and the high precision of MOLLI. T_2-preped bSSFP T_2 mapping can in turn suffer from reduced accuracy due to its sensitivity to noise and B_1 inhomogeneities.[24,47] In PARMANav, the larger number of images and the use of a GRE readout with a complex-valued fitting process help mitigate these issues, resulting in higher accuracy and precision than T_2-prep bSSFP. Techniques such as the abovementioned

MR fingerprinting,[2] and multitasking[4] assess multiple relaxation parameters, removing confounding T_2 effects on T_1 estimation and vice versa. MR fingerprinting has been shown to have improved accuracy after modeling RF pulse imperfections and slice-profile effects,[15] which cannot straightforwardly be added for analytical techniques, but is also incorporated in PARMANav. This may be the main accuracy advantage of dictionary fitting over analytical fitting: imperfections and confounders can be readily added to the fitting process.

Compared to the abovementioned techniques, PARMANav enables free-breathing acquisitions while accounting for through-plane motion, removing another confounder towards increased accuracy and reproducibility. This is largely hypothetical though and should be validated against routine techniques in a multi-center study. Furthermore, there are also contrast mechanism and potential confounders that are not included in PARMANav, such as magnetization transfer (MT)[53] or B_1 inhomogeneity,[15] which may be explored in future studies.

Indeed, in several multiparametric myocardial mapping studies, the radiofrequency (B_1) field was added to the dictionary to improve the T_1–T_2 mapping accuracy. However, these techniques typically use bSSFP readouts with large flip angles, which are known to be more sensitive to B_1 inhomogeneities. For PARMANav we assumed that using GRE readouts and a low flip angle would allow us to ignore B_1 inhomogeneity, but this would be of interest to characterize in a future study. $T_{1\rho}$ relaxation has also increasingly been incorporated in multiparametric techniques,[28,54] but a recent study suggest it does not add information beyond that offered T_1 and T_2 relaxation.[55]

There was no clear trend for wider or narrower NAWW to lead to higher or lower precision or accuracy. This suggests that a NAWW can be chosen purely as a consideration between increased scan time and acceptable through-plane motion. However, the T_1 values of two volunteers with deep breathing pattern were abnormally low for the largest NAWW. This suggests that through-plane motion may cause different tissues to be excited in subsequent heartbeats. As a result, large NAWW should probably be avoided, especially in case of suspected focal disease. Larger NAWW can also lead to a failure of the registration algorithm, which could explain the apparent reduction of the T_1 and T_2 value on the lateral part of the myocardium.

Additional parameters could be experimentally optimized (and reduced) in future studies, such as the flip angle, the number and duration of the preparation modules, or the number of source images. The later was set to 25 to ensure sufficient contrast variations. The free-breathing easily allowed for this high number of images, but it is likely that it can be lowered through a careful optimization study without compromising the precision of the maps. The T_1 CoV could be further reduced by adding a variable flip angle to the images,[28] which would also enable the B_1 field to be mapped.

Dictionary-based multiparametric mapping has several limitations. To limit the size of the dictionary and the associated computation time, a grid of discretized values with a limited size is defined. A too coarse grid will induce discretization errors, while large dictionaries result in long generation and matching times. Parallelization and SVD compression[56] of the dictionary can reduce the computational time. Other limitations of the proposed technique include the difficulty to optimize the sequence, as the navigator rejections might have a larger effect on the contrast variation than the parameter we are looking to optimize.

The main limitation for future integration of the proposed framework in a clinical workflow is the long generation time of the dictionary, which is required for each acquisition. This time would be even higher if this method was extended to include other parameters like B_1. A solution for this issue, as already proposed by Hamilton et al.,[57] would be to train a neural network to generate simulated signals from an acquisition time course.

5 | CONCLUSIONS

We demonstrated that the proposed navigator-gated 2D radial GRE sequence PARMANav allows accurate and precise joint T_1–T_2 mapping during free breathing at 3T. The influence of the navigator acceptance window width on the T_1–T_2 accuracy was found to be minimal, although very large windows could lead to failure of the maps in deep breathers. On the basis of the present results, an acceptance window of ±8 mm was further characterized and applied in three patients as a tradeoff between through-plane motion and acquisition time. Future studies should focus on a clinical validation of this approach, ideally in homogeneous patient cohorts.

FUNDING INFORMATION

This research was supported by the Swiss National Science Foundation (grants 32003B_182615 and CRSII5_202276 to RBvH and PZ00P3_202140 to CWR).

ORCID

Pauline Calarnou https://orcid.org/0000-0003-3273-460X

Augustin C. Ogier https://orcid.org/0000-0001-9178-9964

Christopher W. Roy https://orcid.org/0000-0002-3111-8840

Aurélien Bustin https://orcid.org/0000-0002-2845-8617
Jérôme Yerly https://orcid.org/0000-0003-4347-8613
Ruud B. van Heeswijk https://orcid.org/0000-0001-5028-4521

REFERENCES

1. Ferreira VM, Schulz-Menger J, Holmvang G, et al. Cardiovascular magnetic resonance in nonischemic myocardial inflammation: expert recommendations. *J Am Coll Cardiol*. 2018;72:3158-3176. doi:10.1016/j.jacc.2018.09.072
2. Hamilton JI, Jiang Y, Chen Y, et al. MR fingerprinting for rapid quantification of myocardial T_1, T_2, and proton spin density. *Magn Reson Med*. 2017;77:1446-1458. doi:10.1002/mrm.26216
3. Rumac S, Pavon AG, Hamilton JI, et al. Cardiac MR fingerprinting with a short acquisition window in consecutive patients referred for clinical CMR and healthy volunteers. *Sci Rep*. 2022;12:18705. doi:10.1038/s41598-022-23573-3
4. Christodoulou AG, Shaw JL, Nguyen C, et al. Magnetic resonance multitasking for motion-resolved quantitative cardiovascular imaging. *Nat Biomed Eng*. 2018;2:215-226. doi:10.1038/s41551-018-0217-y
5. Chow K, Hayes G, Flewitt JA, et al. Improved accuracy and precision with three-parameter simultaneous myocardial T1 and T2 mapping using multiparametric SASHA. *Magn Reson Med*. 2022;87:2775-2791. doi:10.1002/mrm.29170
6. Ma D, Gulani V, Seiberlich N, et al. Magnetic resonance fingerprinting. *Nature*. 2013;495:187-192. doi:10.1038/nature11971
7. Eyre K, Lindsay K, Razzaq S, Chetrit M, Friedrich M. Simultaneous multi-parametric acquisition and reconstruction techniques in cardiac magnetic resonance imaging: basic concepts and status of clinical development. *Front Cardiovasc Med*. 2022;9:953823. doi:10.3389/fcvm.2022.953823
8. Liu Y, Hamilton J, Rajagopalan S, Seiberlich N. Cardiac magnetic resonance fingerprinting: technical overview and initial results. *JACC Cardiovasc Imaging*. 2018;11:1837-1853. doi:10.1016/j.jcmg.2018.08.028
9. Ogier AC, Bustin A, Cochet H, Schwitter J, van Heeswijk RB. The road toward reproducibility of parametric mapping of the heart: a technical review. *Front Cardiovasc Med*. 2022;9:876475. doi:10.3389/fcvm.2022.876475
10. Jaubert O, Cruz G, Bustin A, et al. T_1, T_2, and fat fraction cardiac MR fingerprinting: preliminary clinical evaluation. *J Magn Reson Imaging*. 2021;53:1253-1265. doi:10.1002/jmri.27415
11. Rajagopalan V, Siva Kumar S, Madabhushi A, et al. Abstract 14232: performance of cardiac magnetic resonance fingerprinting mapping-evaluation by comparison with standard techniques in a large patient population. *Circulation*. 2021;144:A14232. doi:10.1161/circ.144.suppl_1.14232
12. Chow K, Flewitt JA, Green JD, Pagano JJ, Friedrich MG, Thompson RB. Saturation recovery single-shot acquisition (SASHA) for myocardial T_1 mapping. *Magn Reson Med*. 2014;71:2082-2095. doi:10.1002/mrm.24878
13. Kvernby S, Warntjes MJB, Haraldsson H, Carlhäll CJ, Engvall J, Ebbers T. Simultaneous three-dimensional myocardial T_1 and T_2 mapping in one breath hold with 3D-QALAS. *J Cardiovasc Magn Reson*. 2014;16:102. doi:10.1186/s12968-014-0102-0
14. Blume U, Lockie T, Stehning C, et al. Interleaved T_1 and T_2 relaxation time mapping for cardiac applications. *J Magn Reson Imaging*. 2009;29:480-487. doi:10.1002/jmri.21652
15. Hamilton JI, Jiang Y, Ma D, et al. Investigating and reducing the effects of confounding factors for robust T_1 and T_2 mapping with cardiac MR fingerprinting. *Magn Reson Imaging*. 2018;53:40-51. doi:10.1016/j.mri.2018.06.018
16. Xanthis CG, Bidhult S, Kantasis G, Heiberg E, Arheden H, Aletras AH. Parallel simulations for QUAntifying RElaxation magnetic resonance constants (SQUAREMR): an example towards accurate MOLLI T_1 measurements. *J Cardiovasc Magn Reson*. 2015;17:104. doi:10.1186/s12968-015-0206-1
17. Kellman P, Hansen MS. T_1-mapping in the heart: accuracy and precision. *J Cardiovasc Magn Reson*. 2014;16:2. doi:10.1186/1532-429X-16-2
18. Doneva M, Börnert P, Eggers H, Stehning C, Sénégas J, Mertins A. Compressed sensing reconstruction for magnetic resonance parameter mapping. *Magn Reson Med*. 2010;64:1114-1120. doi:10.1002/mrm.22483
19. Tamir JI, Ong F, Anand S, Karasan E, Wang K, Lustig M. Computational MRI with physics-based constraints: application to multi-contrast and quantitative imaging. *IEEE Signal Process Mag*. 2020;37:94-104. doi:10.1109/msp.2019.2940062
20. Cruz G, Jaubert O, Qi H, et al. 3D free-breathing cardiac magnetic resonance fingerprinting. *NMR Biomed*. 2020;33:e4370. doi:10.1002/nbm.4370
21. Dorniak K, Di Sopra L, Sabisz A, et al. Respiratory motion-registered isotropic whole-heart T2 mapping in patients with acute non-ischemic myocardial injury. *Front Cardiovasc Med*. 2021;8:712383. doi:10.3389/fcvm.2021.712383
22. van Heeswijk RB, Piccini D, Feliciano H, Hullin R, Schwitter J, Stuber M. Self-navigated isotropic three-dimensional cardiac T2 mapping. *Magn Reson Med*. 2015;73:1549-1554. doi:10.1002/mrm.25258
23. Sachs TS, Meyer CH, Hu BS, Kohli J, Nishimura DG, Macovski A. Real-time motion detection in spiral MRI using navigators. *Magn Reson Med*. 1994;32:639-645. doi:10.1002/mrm.1910320513
24. van Heeswijk RB, Feliciano H, Bongard C, et al. Free-breathing 3 T magnetic resonance T_2-mapping of the heart. *JACC Cardiovasc Imaging*. 2012;5:1231-1239. doi:10.1016/j.jcmg.2012.06.010
25. Zhu Y, Kang J, Duan C, et al. Integrated motion correction and dictionary learning for free-breathing myocardial T_1 mapping. *Magn Reson Med*. 2019;81:2644-2654. doi:10.1002/mrm.27579
26. Ludwig J, Kerkering KM, Speier P, Schaeffter T, Kolbitsch C. Pilot tone-based prospective correction of respiratory motion for free-breathing myocardial T_1 mapping. *Magma*. 2023;36:135-150. doi:10.1007/s10334-022-01032-4
27. van Heeswijk RB, Bonanno G, Coppo S, Coristine A, Kober T, Stuber M. Motion compensation strategies in magnetic resonance imaging. *Crit Rev Biomed Eng*. 2012;40:99-119. doi:10.1615/CritRevBiomedEng.v40.i2.20
28. Lyu Z, Hua S, Xu J, et al. Free-breathing simultaneous native myocardial T_1, T_2 and $T_1\rho$ mapping with Cartesian acquisition and dictionary matching. *J Cardiovasc Magn Reson*. 2023;25:63. doi:10.1186/s12968-023-00973-6
29. Wang Y, Riederer SJ, Ehman RL. Respiratory motion of the heart: kinematics and the implications for the spatial

resolution in coronary imaging. *Magn Reson Med*. 1995;33:713-719. doi:10.1002/mrm.1910330517

30. Moghari MH, Hu P, Kissinger KV, et al. Subject-specific estimation of respiratory navigator tracking factor for free-breathing cardiovascular MR. *Magn Reson Med*. 2012;67:1665-1672. doi:10.1002/mrm.23158
31. Yerly J, Ginami G, Nordio G, et al. Coronary endothelial function assessment using self-gated cardiac cine MRI and k-t sparse SENSE. *Magn Reson Med*. 2016;76:1443-1454. doi:10.1002/mrm.26050
32. Henningsson M. Cartesian dictionary-based native T_1 and T_2 mapping of the myocardium. *Magn Reson Med*. 2022;87:2347-2362. doi:10.1002/mrm.29143
33. Di Sopra L, Roy CW, Bastiaansen JAM, et al. Fully self-gated cardiac and respiratory motion-resolved isotropic 5D T_1 mapping of the heart: preliminary results: Proceedings of the International Society for Magnetic Resonance in Medicine. Montréal QC, Canada; 2019.
34. Malik SJ, Padormo F, Price AN, Hajnal JV. Spatially resolved extended phase graphs: modeling and design of multipulse sequences with parallel transmission. *Magn Reson Med*. 2012;68:1481-1494. doi:10.1002/mrm.24153
35. Bustin A, Toupin S, Sridi S, et al. Endogenous assessment of myocardial injury with single-shot model-based non-rigid motion-corrected T_1 rho mapping. *J Cardiovasc Magn Reson*. 2021;23:119. doi:10.1186/s12968-021-00781-w
36. Huizinga W, Poot DHJ, Guyader JM, et al. PCA-based groupwise image registration for quantitative MRI. *Med Image Anal*. 2016;29:65-78. doi:10.1016/j.media.2015.12.004
37. Horn BKP, Schunck BG. Determining optical flow. *Artif Intell*. 1981;17:185-203. doi:10.1016/0004-3702(81)90024-2
38. Wissmann L, Santelli C, Segars WP, Kozerke S. MRXCAT: Realistic numerical phantoms for cardiovascular magnetic resonance. *J Cardiovasc Magn Reson*. 2014;16:63. doi:10.1186/s12968-014-0063-3
39. Roy CW, Heerfordt J, Piccini D, et al. Motion compensated whole-heart coronary cardiovascular magnetic resonance angiography using focused navigation (fNAV). *J Cardiovasc Magn Reson*. 2021;23:33. doi:10.1186/s12968-021-00717-4
40. Stupic KF, Ainslie M, Boss MA, et al. A standard system phantom for magnetic resonance imaging. *Magn Reson Med*. 2021;86:1194-1211. doi:10.1002/mrm.28779
41. Messroghli DR, Radjenovic A, Kozerke S, Higgins DM, Sivananthan MU, Ridgway JP. Modified look-locker inversion recovery (MOLLI) for high-resolution T_1 mapping of the heart. *Magn Reson Med*. 2004;52:141-146. doi:10.1002/mrm.20110
42. Giri S, Chung YC, Merchant A, et al. T2 quantification for improved detection of myocardial edema. *J Cardiovasc Magn Reson*. 2009;11:56. doi:10.1186/1532-429X-11-56
43. Arheden H, Saeed M, Higgins CB, et al. Measurement of the distribution volume of Gadopentetate Dimeglumine at Echo-planar MR imaging to quantify myocardial infarction: comparison with 99mTc-DTPA autoradiography in rats. *Radiology*. 1999;211:698-708. doi:10.1148/radiology.211.3.r99jn41698
44. Meyer P, Rocca A, Banus J, et al. The HeartMagic prospective observational study protocol – characterizing subtypes of heart failure with preserved ejection fraction. *medRxiv*. 2025:25325567. doi:10.1101/2025.04.10.25325567
45. Cerqueira MD, Weissman NJ, Dilsizian V, et al. Standardized myocardial segmentation and nomenclature for tomographic imaging of the heart. *Circulation*. 2002;105:539-542. doi:10.1161/hc0402.102975
46. Messroghli DR, Moon JC, Ferreira VM, et al. Clinical recommendations for cardiovascular magnetic resonance mapping of T_1, T_2, T_2* and extracellular volume: a consensus statement by the Society for Cardiovascular Magnetic Resonance (SCMR) endorsed by the European Association for Cardiovascular Imaging (EACVI). *J Cardiovasc Magn Reson*. 2017;19:75. doi:10.1186/s12968-017-0389-8
47. Akçakaya M, Basha TA, Weingärtner S, Roujol S, Berg S, Nezafat R. Improved quantitative myocardial T_2 mapping: impact of the fitting model. *Magn Reson Med*. 2015;74:93-105. doi:10.1002/mrm.25377
48. Kim D, Cauley SF, Nayak KS, Leahy RM, Haldar JP. Region-optimized virtual (ROVir) coils: localization and/or suppression of spatial regions using sensor-domain beamforming. *Magn Reson Med*. 2021;86:197-212. doi:10.1002/mrm.28706
49. Engblom H, Kanski M, Kopic S, et al. Importance of standardizing timing of hematocrit measurement when using cardiovascular magnetic resonance to calculate myocardial extracellular volume (ECV) based on pre- and post-contrast T_1 mapping. *J Cardiovasc Magn Reson*. 2018;20:46. doi:10.1186/s12968-018-0464-9
50. Hilderink JM, Klinkenberg LJJ, Aakre KM, et al. Within-day biological variation and hour-to-hour reference change values for hematological parameters. *Clin Chem Lab Med*. 2017;55:1013-1024. doi:10.1515/cclm-2016-0716
51. Roujol S, Weingärtner S, Foppa M, et al. Accuracy, precision, and reproducibility of four T_1 mapping sequences: a head-to-head comparison of MOLLI, ShMOLLI, SASHA, and SAPPHIRE. *Radiology*. 2014;272:683-689. doi:10.1148/radiol.14140296
52. Zhang Q, Werys K, Popescu IA, et al. Quality assurance of quantitative cardiac T_1-mapping in multicenter clinical trials – a T_1 phantom program from the hypertrophic cardiomyopathy registry (HCMR) study. *Int J Cardiol*. 2021;330:251-258. doi:10.1016/j.ijcard.2021.01.026
53. Xanthis CG, Bidhult S, Greiser A, et al. Simulation-based quantification of native T_1 and T_2 of the myocardium using a modified MOLLI scheme and the importance of magnetization transfer. *Magn Reson Imaging*. 2018;48:96-106. doi:10.1016/j.mri.2017.12.020
54. Velasco C, Cruz G, Lavin B, et al. Simultaneous T_1, T_2, and $T_1\rho$ cardiac magnetic resonance fingerprinting for contrast agent-free myocardial tissue characterization. *Magn Reson Med*. 2022;87:1992-2002. doi:10.1002/mrm.29091
55. Pang Y. Deciphering adiabatic rotating frame relaxometry in biological tissues. *Magn Reson Med*. 2024;92:2670-2682. doi:10.1002/mrm.30240
56. McGivney DF, Pierre E, Ma D, et al. SVD compression for magnetic resonance fingerprinting in the time domain. *IEEE Trans Med Imaging*. 2014;33:2311-2322. doi:10.1109/TMI.2014.2337321
57. Hamilton JI, Seiberlich N. Machine learning for rapid magnetic resonance fingerprinting tissue property quantification. *Proc IEEE*. 2020;108:69-85. doi:10.1109/JPROC.2019.2936998
58. Stanisz GJ, Odrobina EE, Pun J, et al. T_1, T_2 relaxation and magnetization transfer in tissue at 3T. *Magn Reson Med*. 2005;54:507-512. doi:10.1002/mrm.20605

SUPPORTING INFORMATION

Additional supporting information may be found in the online version of the article at the publisher's website.

Figure S1. Maps of the numerical simulations without noise and the influence of skipped heartbeats. The same measurements as those in Figure 2 are presented here for the noise-free case. No large influence of the number of skipped heartbeats on the myocardial relaxation times or coefficient of variation (CoV) is observed.

Figure S2. PArametric Radial Mapping with Navigator gating (PARMANav) acquisition times as a function of navigator acceptance window width (NAWW). As expected, the acquisition time decreases with larger NAWW.

Table S1. Input T_1 and T_2 values used in the numerical torso simulation. These reference values were previously published by Staniz et al.[58]

How to cite this article: Calarnou P, Ogier AC, Roy CW, et al. Navigator-gated free-breathing 2D radial cardiac joint T_1–T_2 mapping. *Magn Reson Med*. 2025;1-15. doi: 10.1002/mrm.30588